Group velocity dispersion in terahertz frequency combs within a generalized Maxwell-Bloch framework

Lukas Seitner, Johannes Popp, Michael Riesch, Michael Haider, and Christian Jirauschek

Department of Electrical and Computer Engineering, Technical University of Munich, Arcisstr. 21, 80333 Munich, Germany

E-mail: `lukas.seitner@tum.de`

Abstract. As many molecules have their rotovibrational resonance frequencies in the mid-infrared or terahertz regime, efficient generation of corresponding frequency combs may lead to large progress in gas spectroscopy and sensing. Quantum cascade lasers (QCLs) are among the most promising candidates for a compact and cheap radiation source in this frequency range. This contribution presents a full-wave numerical solution of the Maxwell-Liouville-von Neumann equations, thus avoiding the limited applicability of the rotating wave approximation to moderate field strengths and spectral bandwidths. We include losses and chromatic dispersion of the optically active material in the QCL. The semiclassical approach uses the finite-difference time-domain (FDTD) method to derive update equations for the electric field, starting from the one-dimensional Maxwell equations. There, the optical full-wave propagation is coupled to the electronic quantum system via a polarization term that arises from the evolution of the density matrix. Furthermore, dispersion effects are considered through a classical polarization term and losses are introduced by a finite material conductivity. This work mainly focuses on the integration of group velocity dispersion (GVD) due to the bulk material and, if applicable, the waveguide geometry into the update equations. It is known to be one of the main degradation mechanisms of terahertz frequency combs, but has not yet been added to the existing full-wave solver. The implementation is carried out as Lorentz model and is applied to an experimentally investigated QCL frequency comb setup from the literature. The reported results are in good agreement with the experimental data. Especially, they confirm the need for dispersion compensation for the generation of terahertz frequency combs in QCLs.

1. Introduction

Due to the rapid evolution of solid-state optoelectronic devices the demand for predictive simulation software of these systems increases naturally. The recently presented open-source tool mbsolve [1] enables rapid full-wave device modeling. The underlying physical description consists of the Maxwell-Bloch equations, as they are suitable to model light-matter interactions, even in nonlinear regimes [2, 3]. They offer a semiclassical framework, where a propagating electromagnetic wave is described classically by the Maxwell's equations, whereas the electronic system is described in a quantum mechanical framework using the density operator. The temporal evolution of the density operator is governed by the Liouville-von Neumann equation [4]. The Maxwell equations and the Liouville-von Neumann equation are

coupled by the material polarization that depends on the quantum state and changes the optical properties for the solution of the classical field. For a simple two-level system, the von Neumann equation reduces to the Bloch equations, which can be solved more efficiently. However, the simulation of more realistic devices requires the extension to multiple quantum levels, where we solve for the complete density operator in a generalized Maxwell-Bloch approach using the full quantum Liouville equation. This extension has been proven suitable for the simulation of more sophisticated structures [4,5]. Among many different possible systems the most prominent ones are quantum dots (QDs) and quantum cascade lasers (QCLs) [6,7]. In recent years, a lot of effort has been put into the development and refinement of efficient numerical solvers in the Maxwell-Bloch framework, in order to study these devices [8–20].

Often the rotating wave approximation (RWA) and the slowly varying envelope approximation (SVEA) are used to achieve a significant reduction of the numerical workload [3, 4]. However, for certain applications, like the description of ultrashort pulses in optical waveguides [21] or octave-spanning QCL frequency combs [22], the approximations may omit crucial features [23]. Therefore, the mbsolve project avoids to invoke these assumptions in order to properly account for all possible dynamics [1].

A further assumption which is often made is to treat the background refractive index of a material as a constant, while in reality, however, it is a frequency dependent quantity [2]. Therefore, the effect that different frequency components of the electromagnetic wave travel with different velocities, also called group velocity dispersion (GVD), gets neglected. In the current implementation of mbsolve [24], background material dispersion is not explicitly included. Unfortunately, this effect is known to be one of the main degradation mechanisms of frequency comb formation in QCLs [25,26]. Thus, in the contribution at hand, we include a suiting model of group velocity dispersion to the existing solver, in order to apply it to a well studied QCL structure and discuss the influence on terahertz frequency comb formation. It is shown that proper dispersion modeling indeed accounts for degradation in the comb formation, which is in good agreement with experimental evidence [27]. Further, it should be noted that also dispersion due to the waveguide geometry can be accounted for in this approach by using suitably adapted GVD parameters.

In section 2 we introduce our theoretical model for the group velocity dispersion, as well as the Maxwell and Liouville-von Neumann equations. We then derive the update equation for the electric field containing the dispersion formulation. The physical structure of the exemplary QCL frequency comb is given in terms of its electronic potential and the corresponding wavefunctions in section 3. Simulation results that demonstrate the influence of dispersion on terahertz frequency comb generation are presented. Finally, in section 4 we summarize our results and conclude the contribution.

2. Theoretical model

Group velocity dispersion arises from a frequency dependent refractive index, or equivalently, a frequency dependent relative permittivity within a waveguiding material. In this section we present a dispersion model, as well as a concept for coupling it to the generalized Maxwell-Bloch approach. Subsequently, we outline its numerical treatment using the finite-difference time-domain (FDTD) method.

2.1. Spectral permittivity function

In order to describe the variable relative permittivity, an analytic function in the spectral domain can be defined. Here, several models exist which are used in different applications [28]. The most common ones are the Debye, Drude and Lorentz models, which should be selected depending on the conductivity of the respective material. More recently developed dispersion models include the quadratic-complex rational function (QCRF), complex conjugate pole-residue (CCPR), and

the critical point (CP) technique [29]. In this work we decided to use the Lorentz model, as it is a fairly simple but sufficient description of dispersion in slightly n-doped semiconductors (around $1 \times 10^{15}\,\mathrm{cm}^{-3}$). For doping concentrations that are by orders of magnitude larger, a change to the Drude model or an extension to a Drude-Lorentz model should be considered [30]. The low doping requirement of the Lorentz model is typically met in optoelectronic devices, however, our implementation will allow to easily change to a different model.

The Lorentz formulation of the spectral permittivity function is given as

$$\varepsilon_{\mathrm{r}}(\omega) = \varepsilon_{\mathrm{r},\infty} + \chi(\omega) = \varepsilon_{\mathrm{r},\infty} + \frac{\Delta\varepsilon\omega_0^2}{\omega_0^2 - 2\mathrm{i}\omega\delta - \omega^2}\,, \tag{1}$$

where $\chi(\omega)$ is the material susceptibility and $\Delta\varepsilon = \varepsilon_{\mathrm{r},\mathrm{s}} - \varepsilon_{\mathrm{r},\infty}$ is the difference of the static relative permittivity $\varepsilon_{\mathrm{r},\mathrm{s}}$ and the relative permittivity at infinite frequency $\varepsilon_{\mathrm{r},\infty}$. The other two parameters refer to the resonance frequency ω_0 and a damping constant δ. Equation (1) possesses two complex conjugate poles, with a positive and negative resonance frequency, respectively. Physically they refer to a resonant phonon excitation in the material at ω_0, which leads to the absorption of light [30].

The generalized Maxwell-Bloch formalism, however, is defined in time domain. Thus, we seek a temporal representation of the spectral function in order to integrate it to the current implementation of mbsolve. This can be done by introducing a classical polarization term P_{class} in Maxwell's equations. This approach arises from the general identity for the polarization $P = \varepsilon_0 \chi E$. Finally, after an inverse Fourier transformation the Lorentz function will be distributed to coefficients within the update equation for the electric field using the FDTD method.

2.2. Generalized 1D Maxwell-Bloch formalism

With a suitable dispersion model at hand, the generalized Maxwell-Bloch equations shall be discussed briefly. In three dimensions the coupling of Maxwell's equations to the Liouville-von Neumann equation turns out to be rather complex. However, for typical optoelectronic devices we can separate transversal and longitudinal modes within a waveguide and thus it is sufficient to solely consider the propagation direction of the optical field [1, 4]. In a coordinate system where x is the propagation direction and y and z are the transversal coordinates, we can identify $E_z(x,t)$ and $H_y(x,t)$ as the descriptive field components. It is then possible to reduce Maxwell's equations to a time evolution equation of the electric field, given by

$$\partial_t E_z = \varepsilon^{-1}\left(-\sigma E_z - \Gamma\partial_t P_{z,\mathrm{qm}} - \partial_t P_{z,\mathrm{class}} + \partial_x H_y\right), \tag{2}$$

and a time evolution equation of the magnetic field

$$\partial_t H_y = \mu^{-1}\partial_x E_z\,. \tag{3}$$

There, ε and μ represent the total material permittivity and permeability, respectively. The two classical contributions, $P_{z,\mathrm{class}}$ and σE_z, model the polarization caused by bulk and waveguide dispersion as well as the material losses. The interaction of the optical field with the quantum system is given by the term $\Gamma\partial_t P_{z,\mathrm{qm}}$. The overlap factor $\Gamma \in [0,1]$ accounts for the ratio of the spatial overlap between the field and the quantum system. Finally, $\partial_t P_{z,\mathrm{qm}}$ is the temporal derivative of a polarization which arises from the time evolution of the density operator

$$\partial_t P_{z,\mathrm{qm}} = n_{\mathrm{3D}}\,\mathrm{tr}\{\hat{\mu}_z\partial_t\hat{\rho}\}\,, \tag{4}$$

where the density operator itself is governed by the Liouville-von Neumann master equation

$$\partial_t\hat{\rho} = -\mathrm{i}\hbar^{-1}[\hat{H}_0 - \hat{\mu}_z E_z, \hat{\rho}] + \mathcal{D}(\hat{\rho})\,. \tag{5}$$

For more details, we refer to [1].

2.3. Numerical Treatment

As the inclusion of group velocity dispersion affects the classical Maxwell equations, the FDTD update equations for the electromagnetic field need to be modified. In order to derive update equations that can be implemented numerically, we apply the centered differencing scheme to equations (2) and (3). The discrete spatial and temporal indices are denoted by m and n, respectively. The spatial discretization length is given by Δx and time is discretized in multiples of Δt. The electric field E_z at the next timestep $n+1$ at a certain location m is given by

$$E_z^{m,n+1} = aE_z^{m,n} + b\left[\frac{1}{\Delta x}\left(H_y^{m+\frac{1}{2},n+\frac{1}{2}} - H_y^{m-\frac{1}{2},n+\frac{1}{2}}\right) - \Gamma\partial_t P_{z,\mathrm{qm}}^{m,n+\frac{1}{2}}\right]$$
$$- d\left(P_{z,\mathrm{class}}^{m,n+1} - P_{z,\mathrm{class}}^{m,n}\right) \tag{6}$$

with the coefficients

$$a = \frac{2\varepsilon - \sigma\Delta t}{2\varepsilon + \sigma\Delta t}, \qquad b = \frac{2\Delta t}{2\varepsilon + \sigma\Delta t}, \qquad d = \frac{2}{2\varepsilon + \sigma\Delta t}.$$

The magnetic field update equation results in

$$H_y^{m+\frac{1}{2},n+\frac{1}{2}} = H_y^{m+\frac{1}{2},n-\frac{1}{2}} + \frac{\Delta t}{\Delta x\mu}\left(E_z^{m+1,n} - E_z^{m,n}\right). \tag{7}$$

The field components E_z and H_y as well as the density operator $\hat{\rho}$ lie on a Yee grid, where the respective electric and magnetic field grids are shifted by half a discretization length [1]. Note that the temporal derivative of the quantum mechanical polarization in (6) is not discretized intentionally. The mbsolve subroutine for the time evolution of the density operator explicitly returns the time derivate of the polarization induced by the quantum system.

Notably, the calculated electric field $E_z^{m,n+1}$ depends on the polarization at the same timestep $P_{z,\mathrm{class}}^{m,n+1}$, which prevents direct updating at this point. Therefore, we use the relation $P(\omega) = \varepsilon_0\chi(\omega)E(\omega)$ and apply the inverse Fourier-transform and centered-differencing scheme to obtain an update equation for the classical polarization [29]

$$P_{z,\mathrm{class}}^{m,n+1} = \frac{C_\mathrm{d}}{C_\mathrm{a}}E_z^{m,n+1} + \frac{C_\mathrm{e}}{C_\mathrm{a}}E_z^{m,n} + \frac{C_\mathrm{f}}{C_\mathrm{a}}E_z^{m,n-1} - \frac{C_\mathrm{b}}{C_\mathrm{a}}P_{z,\mathrm{class}}^{m,n} - \frac{C_\mathrm{c}}{C_\mathrm{a}}P_{z,\mathrm{class}}^{m,n-1}. \tag{8}$$

Equation (8) contains the information of the spectral permittivity function (1) about the group velocity dispersion in the prefactors C_j/C_a with $j \in \{\mathrm{b,c,d,e,f}\}$. The coefficients have the following values [29]:

$$\begin{aligned}
&C_\mathrm{a} = 2(1 + \delta\Delta t), &&C_\mathrm{b} = 2\omega_0^2\Delta t^2 - 4, &&C_\mathrm{c} = 2(1 - \delta\Delta t), \\
&C_\mathrm{d} = 0, &&C_\mathrm{e} = 2\Delta\varepsilon\omega_0^2\varepsilon_0\Delta t^2, &&C_\mathrm{f} = 0.
\end{aligned}$$

Inserting these coefficients into the update equation (6), it is now possible to solve explicitly for $E_z^{m,n+1}$. Due to vanishing C_d and C_f the update equation for the classical polarization is only dependent on values of the previous timestep. It should be noted that this simplification is also valid for the Debye and Drude dispersion models. Starting from our formulation, these two models can be implemented by changing C_a, C_b, C_c, and C_e [29]. Nevertheless, it is useful to keep the factors C_d and C_f at this point as they become relevant for more advanced models (QCRF, CCPR, CP).

Substituting (8) into (6) yields the final update equation for the electric field

$$E_z^{m,n+1} = aE_z^{m,n} + b\left[\frac{1}{\Delta x}\left(H_y^{m+\frac{1}{2},n+\frac{1}{2}} - H_y^{m-\frac{1}{2},n+\frac{1}{2}}\right) - \Gamma\partial_t P_{z,\mathrm{qm}}^{m,n+\frac{1}{2}}\right]$$
$$+ d\left(P_{z,\mathrm{class}}^{m,n} - W_1^{m,n}\right). \tag{9}$$

Here, the non-physical quantity W_1 has been introduced to avoid storing of full field samples of two independent timesteps, which would have been necessary according to $P_{\text{class}}^{m,n-1}$ in (8). This introduction makes the implementation more memory efficient [29]. The quantity W_1 contains information of two timesteps by introducing a second quantity W_2. These two variables are linked to the dispersion polarization term $P_{z,\text{class}}$ by

$$P_{z,\text{class}}^{m,n+1} = W_1^{m,n}, \tag{10}$$

$$W_1^{m,n+1} = \frac{C_{\text{e}}}{C_{\text{a}}} E_z^{m,n+1} - \frac{C_{\text{b}}}{C_{\text{a}}} P_{z,\text{class}}^{m,n+1} + W_2^{m,n}, \tag{11}$$

$$W_2^{m,n+1} = -\frac{C_{\text{c}}}{C_{\text{a}}} P_{z,\text{class}}^{m,n+1}. \tag{12}$$

Notably, in the above equation (11), the coefficient for $E_z^{m,n+1}$ is $\frac{C_{\text{e}}}{C_{\text{a}}}$ while in (8) this is the coefficient of $E_z^{m,n}$. This is due to the fact that the electric field has already been updated in this timestep and therefore $E_z^{m,n}$ becomes $E_z^{m,n+1}$, while the coefficient stay the same. Thus it is important to carry out the calculations for the electric field and the polarization in the correct order. This form of the update equations has been implemented in mbsolve, however, the project is under active development and thus the equations may change at any time.

In order to assure the correctness of the dispersion implementation we simulated a test scenario described in [28]. In this experiment, the evolution of a hyperbolic secant pulse entering and passing through an exemplary dispersive medium is investigated. The nearly identical results indicate the validity of the implemented method.
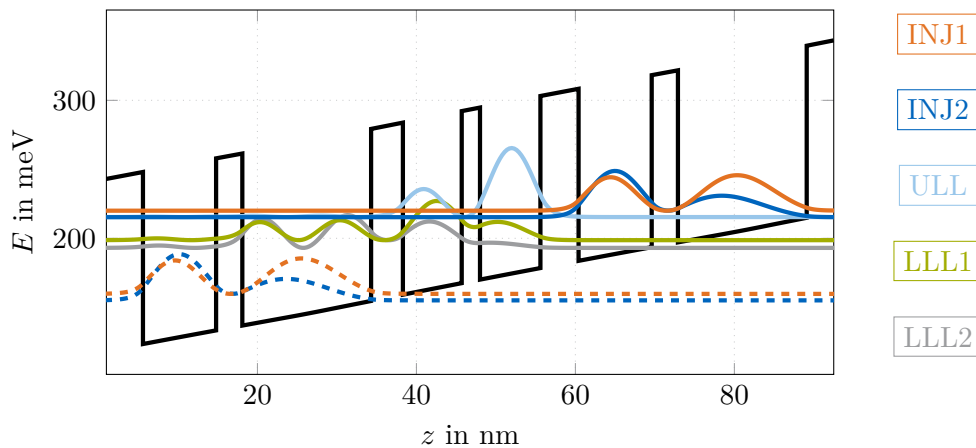
3. Dispersion in QCL frequency combs
After verifying the implementation, the dispersion aware model has been applied to a well studied and experimentally tested QCL frequency comb structure [16, 27]. The simulation setup and the results are presented and discussed in the following.

3.1. Setup for comb generation
In horizontal direction, the optical propagation direction, the cavity length of the QCL frequency comb structure is 5 mm. Along the vertical axis, a QCL typically consists of many identical periods of optically active quantum-well systems [13]. As we wish to reduce the numerical load of our calculations as far as possible, we only consider a single period of the quantum system and apply periodic boundary conditions.

In one period, the physical processes can be modeled by a five-level system. This is visualized in Figure 1, where the potential and associated quantum states of roughly one and a half periods are plotted along the growth direction z. Of the seven states that can be seen in Figure 1, the dashed curves refer to states of the adjacent period. They are taken into account to indicate the periodicity of the system and are equivalent to the solid blue and orange line. These two states serve as injector levels $|\text{INJ1}\rangle$ and $|\text{INJ2}\rangle$. They supply charge carriers to the upper laser level $|\text{ULL}\rangle$ of their respective period. The splitting of these three states is necessary in order to correctly model coherent tunneling through the injector barrier according to the tight binding approximation [13]. At the given bias field of 11 kV/cm, as shown in Figure 1, the eigenenergies of $|\text{INJ2}\rangle$ and $|\text{ULL}\rangle$ assume nearly identical values. We can therefore assume $|\text{INJ2}\rangle$ to be the main injector state [19]. In order to model this asymmetric carrier injection we choose the rate of quantum mechanical dephasing between $|\text{INJ1}\rangle$ and $|\text{ULL}\rangle$ to be $3.33 \times 10^{15}\,\text{s}^{-1}$ which is $\approx 2\,000$ times larger than the rate between $|\text{INJ2}\rangle$ and $|\text{ULL}\rangle$ ($1.67 \times 10^{12}\,\text{s}^{-1}$).

The remaining two energy eigenstates are the lower laser levels $|\text{LLL1}\rangle$ and $|\text{LLL2}\rangle$. However, in our model a dipole moment of $4\,\text{nm} \times e$ only exists from $|\text{ULL}\rangle$ to $|\text{LLL1}\rangle$, where e is the

Figure 1. Potential and according quantum state probability distributions of the investigated QCL structure at a bias field strength of $11\,\mathrm{kV/cm}$.

Table 1. Selected parameters of the Lorentz dispersion model for n-doped gallium arsenide.

$\varepsilon_{\mathrm{r,s}}$	$\varepsilon_{\mathrm{r,\infty}}$	ω_0 in THz	δ in GHz
12.96	10.89	$2\pi\,8.070$	$2\pi\,37.474$

elementary charge. Thus, there is only a single radiative transition at a center frequency of $f = 3.869\,\mathrm{THz}$. Nevertheless, non-radiative transitions from $|\mathrm{ULL}\rangle$ into $|\mathrm{LLL2}\rangle$ remain possible, so they are modeled by a corresponding scattering rate.

In order to achieve laser operation $|\mathrm{LLL1}\rangle$ needs to be efficiently depopulated into the next period, which typically happens by tailored depopulation levels [13]. However, in this case they coincide with the injector levels of the next period. Thus, we obtain scattering rates between the two lower laser levels and the injector levels of the next period.
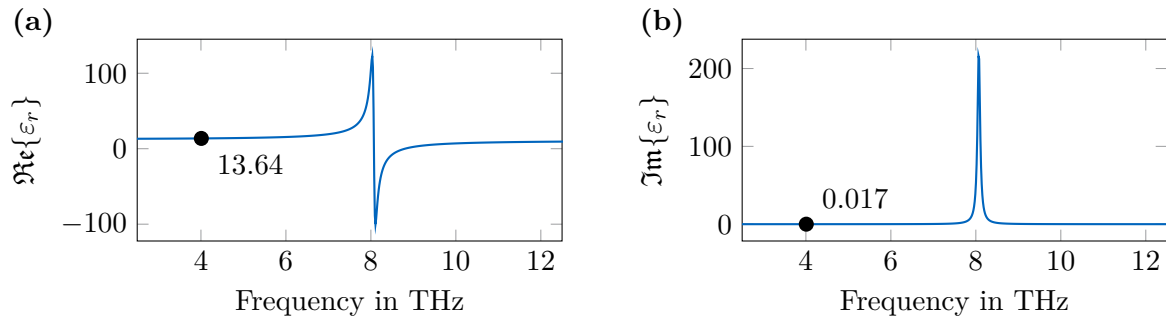
An overview of the included eigenenergies, scattering, and dephasing rates of the quantum mechanical model is given in the appendix. They were extracted by a Schrödinger-Poisson solver and the Ensemble-Monte-Carlo method, respectively.
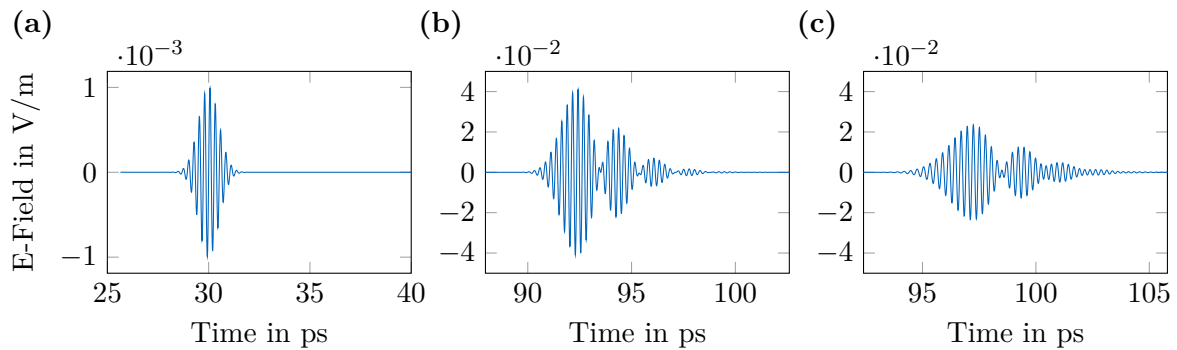
3.2. Dispersion parameter choice

Before simulating the QCL structure, parameters for the Lorentz dispersion model must be chosen carefully, in order to match the gallium arsenide (GaAs) bulk material. The values for the reststrahlen region were extracted from literature [30,31]. An overview of these parameters is shown in Table 1. The frequency dependent permittivity function (1) with the according Lorentz parameters is plotted in Figure 2. We observe that the phononic resonance frequency of the n-doped GaAs lies around 8 THz. Consequently, the operation of a laser at this frequency would be unfeasible. However, also for devices operating close to this pole, like our QCL frequency comb structure ($\approx 4\,\mathrm{THz}$), the varying relative permittivity should be taken into account.

In subfigure 2 (a) the real part of the complex permittivity function is plotted, where the relative permittivity value for a frequency of $4\,\mathrm{THz}$ is highlighted. At this point the relative permittivity has a value of about 13.64 with a positive slope. This will lead to different round trip times for distinct frequency modes in the laser cavity and thus to group velocity dispersion.

The same pole close to $8\,\mathrm{THz}$ can be seen in the imaginary part, depicted in subfigure 2 (b).

(a)

(b)

Figure 2. Real part (a) and imaginary part (b) of the permittivity according to the Lorentz model using the parameters from Table 1.

(a)

(b)

(c)

Figure 3. Gaussian pulses included in the conducted computer experiment. In (a) the excited pulse at the first cavity interface is plotted. The recorded pulse at the second interface is shown in (b) without the explicit dispersion model, and in (c) applying the model.

The imaginary part of the function accounts for additional losses. Therefore, field components with a frequency close to the pole will experience large damping. This also implies that the overall field strength inside the cavity will be smaller compared to the non-dispersive case, while the overall power gets distributed over a broader frequency range.

3.3. Dispersion mechanisms
In order to identify the included dispersion mechanisms, we perform a time-domain pulse distortion simulation. The system is excited with a Gaussian field pulse at one interface of the cavity. The initial pulse, plotted in Figure 3 (a), travels through the medium once (half a cavity round trip) and is finally observed at the other cavity facet. This simulation was conducted twice, once without the inclusion of the newly modeled bulk material and waveguide dispersion (we also call this case "dispersion-free"), and once using the modified update equations. The observed pulse shape, assuming a non-dispersive medium, is given in Figure 3 (b). The one containing waveguide dispersion on the other hand is plotted in Figure 3 (c). The results show that the interaction of the optical field with the quantum system indeed leads to an amplification of the pulse in both cases. We see that in Figure 3 (b), even in the absence of the explicit group velocity dispersion, the initial pulse gets broadened and distorted. This effect can be attributed to the chromatic dispersion caused by the quantum system, which was also observed in previous simulations and experiments. This effect is known to account for the degradation of frequency combs on its own [16, 26, 27].

However, in Figure 3 (c), where we additionally include the classical group velocity dispersion of the gain material, it can be seen that the broadening effect gets more pronounced. This confirms the effects of a longer round trip time and increased damping, predicted in section 3.2. The pulse in Figure 3 (c) is arriving roughly 5 ps later at the second interface as a consequence of the increased real part of the permittivity. The amplified field strength in the case of additional dispersion is smaller, due to damping included in the imaginary part of the relative permittivity.

When putting these results together we notice that two contributions to the overall dispersion are present: one part arising from the interaction of the optical field with the quantum system and the other part from the classical material dispersion, which was added within this work. Experimental results show that a special dispersion grating can be used, such that both contributions roughly cancel each other. This leads to an improved laser performance [27]. In our present work we refrain from modeling this elaborate grating and rather investigate the effect of including the classical material dispersion of bulk GaAs on the frequency comb generation.
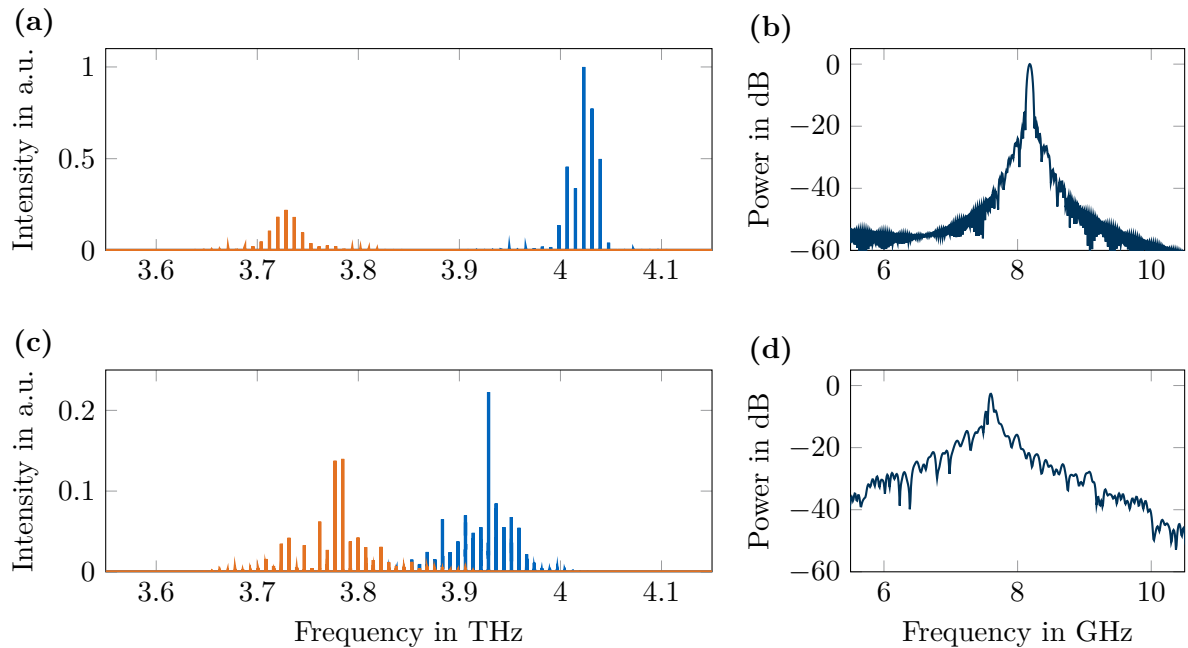
3.4. Frequency comb operation

We now investigate the frequency comb operation properties of the aforementioned device. Therefore, we randomly initialize the electric field with zero mean and a standard deviation of roughly 5×10^{-16} V/m at each grid point within the cavity. For the quantum system we assume nearly perfect population inversion at the beginning to enhance light-matter interaction. The system then evolves for 60 ns, which corresponds to about 500 round trips of the optical field in the cavity. The full-wave electric field strength over time at the interface of the cavity is recorded for further data processing.

3.4.1. Spectral results   The laser enters a steady state operation regime after around 250 round trips. Thus, we Fourier transform the recorded field data starting at that point in time and obtain the output spectrum of the laser. The resulting frequency comb spectra are depicted in Figure 4, again for the "non-dispersive" case (a) and (b), and for the dispersive case (c) and (d). Let us first consider the case, where only dispersion due to the quantum system is present. In Figure 4 (a) it is clearly visible that two distinct frequency comb lobes have formed. The one at lower frequencies, plotted in orange color, has a center frequency of about 3.72 THz and the higher frequency comb, drawn in blue color, builds up around 4.02 THz. The different coloring was chosen to aid the reader in keeping track of the different modes when looking at temporal results. The division of the spectrum is done by applying a bandpass filter to each of the lobes. In this normalized linear intensity plot, we can count about 20 distinct comb modes, where the ones of the higher frequency lobe are clearly dominant. On a logarithmic scale even up to 70 modes can be identified in the considered frequency range. This result matches well to the results of the same structure simulated using the rotating wave approximation [16], also including chromatic dispersion due to the quantum system.

We further consider the RF beatnote of the field at the cavity interface in Figure 4 (b). A prominent peak around 8.1 GHz can be observed. It drops rapidly to -20 dB and for further spaced frequencies even to less than -50 dB. This indicates that the different field modes mainly travel with a similar group velocity. However, here the frequency resolution is limited by the Fourier transform to roughly 16 MHz. A closer investigation of the beatnote would require a far longer simulation time, which is unfeasible using our full-wave approach.

Now we compare the presented results to the case where bulk material and waveguide dispersion gets additionally included. In Figure 4 (c), it is clearly visible that both lobes show a decreased intensity and a broadened spectrum. The intensities in the plot are still normalized to the highest intensity mode of the non-dispersive comb for better comparison. It can be observed that the number of identified modes increased and the power is more equally
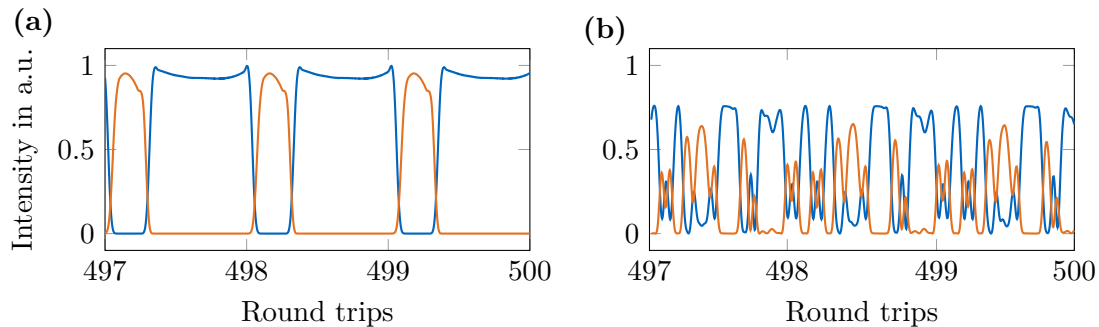
Figure 4. Simulation results of the THz frequency comb and the RF beatnote. In the absence of background and waveguide group velocity dispersion (GVD) two clear and distinct frequency combs (a) and a sharp beatnote (b) arise. When including this kind of GVD, the two combs broaden and loose intensity (c). The beatnote becomes more distorted (d).

distributed. Integrating over all modes delivers roughly the same overall power in both cases (non-dispersive and dispersive).

Finally, we can conclude that through material dispersion additional modes arise which carry parts of the energy of the previous modes. The system behavior becomes more irregular and an efficient generation of the desired comb spectrum gets deteriorated. This argument is supported by the RF beatnote shown in Figure 4 (d). It is obvious that, compared to the case of no waveguide dispersion, more power is distributed to side modes of different round trip frequencies. The most dominant peak is almost $-3\,\mathrm{dB}$ weaker than in Figure 4 (b). The shift of the center frequency to below $8\,\mathrm{GHz}$ can be explained by the increased permittivity due to the pole in the spectral function and the associated longer round trip time.

3.4.2. Time domain results Aside from the spectral results, it is also worthwhile to have a brief look at the time resolved fields, in order to further support the interpretation. In Figure 5 again two plots can be seen, in which the field envelopes are depicted. The included time spans over the last three round trips and the fields refer to (a) the dispersion-free case and (b) to the case of dispersive waveguide material. Notably, the division into orange and blue parts for the lower and higher frequency contributions reappears in these plots. In Figure 5 (a) a clear distinction of the field into the higher and lower frequency lobe can be seen. The fact that the blue lobe dominates the temporal behavior is consistent with the fact that the higher frequency lobe has larger intensity in the spectral plot in Figure 4 (a). Both components are alternating temporally at the cavity interface. This effect has already been observed experimentally, as well as in simulations, and was named "temporal hole burning" [16, 32]. The reason of this behavior is believed to lie in the strong anti-crossing of the injector quantum states.

For the dispersive case shown in Figure 5 (b) we observe decreased intensity and large

Figure 5. Electric field envelope at the interface of the laser cavity for the last three simulated round trips. In absence of bulk and waveguide dispersion (a) a clear temporal separation between the higher and lower frequency lobe is visible. By inclusion of this kind of chromatic dispersion (b) the field is distributed to more modes with less intensity and the clear temporal separation is lifted.

distortions of the envelopes. Again, we normalize the field to the highest intensity achieved in the non-dispersive case. It can be seen that even in the presence of many parasitic modes, the periodicity and exchange of the field components, or "temporal hole burning", is still present. This is not surprising since the explicitly included dispersion model does not directly affect the quantum system but only acts on the propagating field in the cavity.

Nevertheless, these results imply that waveguide dispersion is disadvantageous for stable frequency comb operation. Thus, we can support the assumption that a dispersion compensation grating contained in the waveguide is necessary for THz frequency comb operation [27].

4. Conclusion

In this contribution we presented an extension to the open-source solver tool mbsolve that adds chromatic dispersion due to the bulk material and waveguide geometry. The mathematical formulation of a frequency dependent permittivity could be integrated into the generalized Maxwell-Bloch equation system. Notably, it is possible to replace the Lorentz dispersion model considered for the present paper by several other models at comparably low effort. In order to validate our extension, we simulated a terahertz frequency comb QCL structure using the modified update equations. The results showed that the added group velocity dispersion leads to a degradation of frequency comb formation, which coincides with experiments and common literature. The presented work can be used to predict the performance of quantum-optical devices more accurately. In particular, this allows to engineer chromatic dispersion due to the bulk material and waveguide geometry such that it compensates for other dispersion mechanisms, e.g. by choosing a waveguide design with an integrated grating. With this, we hope to be able to contribute to the improvement of quantum-optoelectronic devices.

Appendix

Table A1. Energies of the five eigenstates in a single QCL period at a bias field of $11\,\mathrm{kV/cm}$.

$|\mathrm{INJ1}\rangle$	$|\mathrm{INJ2}\rangle$	$|\mathrm{ULL}\rangle$	$|\mathrm{LLL1}\rangle$	$|\mathrm{LLL2}\rangle$
$4.065\,\mathrm{meV}$	$0\,\mathrm{eV}$	$0\,\mathrm{eV}$	$-0.016\,\mathrm{eV}$	$-0.021\,\mathrm{eV}$

Table A2. Scattering rates between states ($\times 10^{12}\,\mathrm{s}^{-1}$).

	$|\mathrm{INJ1}\rangle$	$|\mathrm{INJ2}\rangle$	$|\mathrm{ULL}\rangle$	$|\mathrm{LLL1}\rangle$	$|\mathrm{LLL2}\rangle$
$|\mathrm{INJ1}\rangle$	0	0.495	0.097	0.812	1.041
$|\mathrm{INJ2}\rangle$	0.825	0	0.136	0.662	1.124
$|\mathrm{ULL}\rangle$	0.023	0.047	0	0.079	0.036
$|\mathrm{LLL1}\rangle$	0.005	0.003	0.125	0	0.281
$|\mathrm{LLL2}\rangle$	0.005	0.005	0.110	0.495	0

Table A3. Additional simulation parameters.

Parameter	Value
Lin. amplitude loss	$11\,\mathrm{cm}^{-1}$
Avg. carrier density	$5.6 \times 10^{15}\,\mathrm{cm}^{-3}$
Overlap factor	0.9
Mirror reflectivity	0.8
Anti-crossing energy $|\mathrm{INJ1}\rangle \leftrightarrow |\mathrm{ULL}\rangle$	$1.18\,\mathrm{meV}$
Anti-crossing energy $|\mathrm{INJ2}\rangle \leftrightarrow |\mathrm{ULL}\rangle$	$1.38\,\mathrm{meV}$

References

[1] Riesch M and Jirauschek C 2021 *Comput. Phys. Commun.* **268** 108097
[2] Boyd R W 2020 *Nonlinear Optics* 4th ed (Academic press) ISBN 9780323850575
[3] Allen L and Eberly J H 1987 *Optical Resonance and Two-Level Atoms* vol 28 (Courier Corporation) ISBN 0-486-65533-4
[4] Jirauschek C, Riesch M and Tzenov P 2019 *Adv. Theory Simul.* **2** 1900018
[5] Hioe F T and Eberly J H 1981 *Phys. Rev. Lett.* **47**(12) 838–841
[6] Kirstaedter N, Ledentsov N N, Grundmann M, Bimberg D, Ustinov V M, Ruvimov S S, Maximov M V, Kopév P S, Alferov Z I, Richter U, Werner P, Gösele U and Heydenreich J 1994 *Electron. Lett.* **30** 1416–1417
[7] Faist J, Capasso F, Sivco D L, Sirtori C, Hutchinson A L and Cho A Y 1994 *Science* **264** 553–556
[8] Slavcheva G 2008 *Phys. Rev. B* **77**(11) 115347
[9] Menyuk C R and Talukder M A 2009 *Phys. Rev. Lett.* **102**(2) 023903
[10] Choi H, Gkortsas V M, Diehl L, Bour D, Corzine S, Zhu J, Höfler G, Capasso F, Kärtner F X and Norris T B 2010 *Nat. Photonics* **4** 706–710

[11] Gkortsas V M, Wang C, Kuznetsova L, Diehl L, Gordon A, Jirauschek C, Belkin M A, Belyanin A, Capasso F and Kärtner F X 2010 *Opt. Express* **18** 13616–13630

[12] Freeman J R, Maysonnave J, Khanna S, Linfield E H, Davies A G, Dhillon S S and Tignon J 2013 *Phys. Rev. A* **87**(6) 063817

[13] Jirauschek C and Kubis T 2014 *Appl. Phys. Rev.* **1** 011307

[14] Talukder M A and Menyuk C R 2014 *Opt. Express* **22** 15608–15617

[15] Wang Y and Belyanin A 2015 *Opt. Express* **23** 4173–4185

[16] Tzenov P, Burghoff D, Hu Q and Jirauschek C 2016 *Opt. Express* **24** 23232–23247

[17] Cartar W, Mørk J and Hughes S 2017 *Phys. Rev. A* **96**(2) 023859

[18] Vuković N N, Radovanović J, Milanović V and Boiko D L 2017 *IEEE J. Sel. Top. Quantum Electron.* **23** 1200616

[19] Jirauschek C and Tzenov P 2017 *Opt. Quant. Electron.* **49** 414

[20] Slavcheva G, Koleva M and Rastelli A 2019 *Phys. Rev. B* **99**(11) 115433

[21] Slavcheva G, Arnold J M, Wallace I and Ziolkowski R W 2002 *Phys. Rev. A* **66**(6) 063418

[22] Rösch M, Scalari G, Beck M and Faist J 2015 *Nat. Photonics* **9** 42–47

[23] Ziolkowski R W, Arnold J M and Gogny D M 1995 *Phys. Rev. A* **52**(4) 3082–3094

[24] Riesch M and Jirauschek C 2021 mbsolve: An open-source solver tool for the Maxwell-Bloch equations https://github.com/mriesch-tum/mbsolve

[25] Villares G and Faist J 2015 *Opt. Express* **23** 1651–1669

[26] Tzenov P, Burghoff D, Hu Q and Jirauschek C 2017 *IEEE Trans. Terahertz Sci. Technol.* **7** 351–359

[27] Burghoff D, Kao T Y, Han N, Chan C W I, Cai X, Yang Y, Hayton D J, Gao J R, Reno J L and Hu Q 2014 *Nat. Photonics* **8** 462–467

[28] Taflove A and Hagness S C 2005 *Computational Electrodynamics: The Finite-Difference Time-Domain Method* 3rd ed (Artech House, Boston) ISBN 1-58053-832-0

[29] Choi H, Baek J W and Jung K Y 2019 *IEEE Trans. Antennas Propag.* **67** 7643–7648

[30] Chochol J, Postava K, Čada M, Vanwolleghem M, Mičica M, Halagačka L, Lampin J F and Pištora J 2017 *J. Eur. Opt. Soc.-Rapid Publ.* **13** 13

[31] Adachi S 1999 *Optical Properties of Crystalline and Amorphous Semiconductors: Materials and Fundamental Principles* (Springer Science & Business Media, New York) ISBN 978-1-4613-7389-6

[32] Burghoff D, Yang Y, Hayton D J, Gao J R, Reno J L and Hu Q 2015 *Opt. Express* **23** 1190–1202